



Fabrication of FePt nanowires through pulsed electrodeposition into nanoporous alumina templates

R. Magalhães^{1,2} · M. P. Proenca^{1,2,3} · J. P. Araújo^{1,2} · C. Nunes⁴ · A. M. Pereira^{1,2} · C. T. Sousa^{1,2}

Received: 25 October 2021 / Accepted: 21 February 2022 / Published online: 6 May 2022
© King Abdulaziz City for Science and Technology 2022

Abstract

One-dimensional magnetic nanostructures have been emerging as promising nanomaterials for biomedical applications. Among those types of nanoarchitectures, FePt nanowires are particularly interesting; since they are highly biocompatible and chemically inert, their magnetic properties can be tuned by controlling not only the atomic ratio of the two elements in the alloy structure but also the nanowire's dimensions, and they have a high magnetic anisotropy. In this work, we report the fabrication of such nanostructures through pulsed electrodeposition into nanoporous aluminium oxide templates. Using this approach, we were able to control the composition of the produced nanoarchitectures by adjusting the thickness of the barrier layer, which is located at the bottom of the template, and the current density applied during the electrodeposition process. The obtained nanostructures exhibited a heterogeneous length distribution when Pt was present. Moreover, their magnetic characterization revealed an increase of the magnetic hysteresis, coercivity, remanence, and saturation field as the Fe atomic percent got higher. Furthermore, hysteresis loops of FePt nanowire arrays were simulated and compared with the experimental measurements. Such comparison suggested that the nanostructures with Pt in their composition might have different stoichiometries along their length.

Keywords Nanomaterials · Nanowires · Electrodeposition · Nanoporous alumina templates · FePt · Micromagnetic simulations

Introduction

According to the World Cancer Report, cancer is the second leading cause of death worldwide, having been responsible for about 9.6 million deaths, i.e. around one-sixth of the deaths globally, in 2018 (Kesari 2019; Spagnuolo 2020; Thorat and Bauer 2020). Currently, various authors have

been interested in developing novel efficient oncological therapies that have less side effects than the conventional oncological treatments (Pucci et al. 2019).

In this line of research, nanomaterials are particularly promising and, among all the types of nanomaterials employed in biomedicine, nanomagnets are one of the most used, mainly due to their low toxicity, biocompatibility, and inducible magnetic moments, which allow their remote control by the application of an external magnetic field (Gao et al. 2014; Casillas et al. 2015). Consequently, there are various biomedical applications where these nanomaterials can be employed, such as cellular therapy involving cell labelling and targeting, separation and purification of cell populations, regenerative medicine, targeted drug delivery, contrast enhancement in magnetic resonance imaging (MRI), hyperthermia, or magnetomechanically induced cell death (Tran and Webster 2010; Chiriac et al. 2018). Furthermore, it is possible to combine diagnostic and treatment capabilities in a single nanomagnet, which, as result, can be used as a theranostic agent (Thanou 2018).

✉ R. Magalhães
rmoboista@gmail.com

¹ Institute of Physics for Advanced Materials, Nanotechnology and Photonics (IFIMUP), Rua do Campo Alegre, 4169-007 Porto, Portugal

² Departamento de Física e Astronomia, Faculdade de Ciências da Universidade do Porto, Rua do Campo Alegre, 4169-007 Porto, Portugal

³ ISOM and Departamento Electrónica Física, Universidad Politécnica de Madrid, Avda. Complutense 30, 28040 Madrid, Spain

⁴ LAQV, REQUIMTE, Faculty of Pharmacy of Porto University, Porto, Portugal

Superparamagnetic nanoparticles (typically made of iron oxide) are one of the most widely studied and used magnetic nanomaterials in biomedicine, principally due to their biocompatibility and zero remanence. The latter is a crucial requirement for the biomedical application of nanomagnets, as it prevents them from agglomerating when dispersed in a solution (Wu et al. 2019; Vashist et al. 2018; Mora et al. 2018).

However, various aspects, such as small net magnetic moment, reduced sensitivity in MRI diagnosis, and low loading capacity, limit the utilization of magnetic nanoparticles (MNPs) in the clinical practice, especially the spherical ones with a superparamagnetic behaviour (Ha et al. 2018; Zhang and Zhao 2017; Xiao and Du 2020). As a result, with the aim of achieving better performances than those of MNPs, there has been emerging an interest for developing new types of nanomaterials that have less limitations (Peixoto 2018; Domracheva et al. 2018). Within this scope, magnetic nanostructures with high aspect ratio (such as nanowires, nanorods, nanotubes, or nanodiscs) are promising candidates, due to their spin configurations and unique properties (Peixoto 2018; Hanusa 2015).

In this context, nanoarchitectures composed of ferromagnetic elements are, naturally, of great interest, since those elements have large magnetic moments and, therefore, such nanoarchitectures typically need magnetic fields with less demanding requirements to achieve effective results (Peixoto 2018; Hanson et al. 2002; Kanaan 2011; Elmiladi 2010). Among the most common ferromagnetic elements, i.e. Ni, Co, and Fe, only Fe is biocompatible, which is a fundamental requirement for the use of nanostructures in the biomedical field (Whitehead 2020; Mansor et al. 2020; Hu et al. 2010; Li 2015). However, Fe oxidizes easily, which can be advantageous for some applications, but in this particular context it is a drawback, since iron oxides have a lower saturation magnetization (Sandaker et al. 2019; Faivre 2016; Janocha 2007; Schwerdt et al. 2012). Therefore, a promising approach for overcoming such problem is the fabrication of nanoarchitectures composed of biocompatible and oxidation-resistant Fe alloys.

Within this scope, nanowires (NWs) composed of FePt are particularly promising; since they have a good biocompatibility, are chemically inert, their magnetic properties can be adjusted by regulating not only the atomic ratio of the two elements in the alloy structure but also the NW's shape and size, and they have a large magnetic anisotropy (Crisan et al. 2020; Kadiri et al. 2020; Wang et al. 2007; Sun et al. 2005; Elkins et al. 2005).

One of the simplest and, therefore, one of the most attractive methods for fabricating one-dimensional nanostructures is template-assisted electrodeposition into self-assembled nanoporous anodic aluminium oxide (PAA) membranes, which allows a precise and easy control of the dimensions,

shape, and composition of the resulting nanoarchitectures, without requiring expensive equipment or lengthy processes (Stepniowski and Salerno 2014; Meier et al. 2015; Ertan et al. 2008; Vega et al. 2012a, b). This technique consists of filling, through electrodeposition, the cylindrical nanopores present in PAA templates with the desired metal (Stepniowski and Salerno 2014; Meier et al. 2015).

There are various electrodeposition methods that can be employed to grow the nanoarchitectures in the nanoholes of a PAA template (Jokar et al. 2016). A particularly interesting one is pulsed electrodeposition (PED), where the aluminium substrate is used as the cathode and a modulated signal, composed of three successive electric pulses, is applied to plate the desired material from an electrolyte containing the desired ions to be deposited (Azevedo et al. 2012; Mota et al. 2020). However, prior to the deposition process, the thickness of the aluminium oxide (alumina) barrier layer, present at the bottom of the nanopores, has to be reduced. This is performed through a non-steady-state anodization, where the anodization potential is exponentially decreased (Sousa et al. 2012a; Azevedo et al. 2014; Nielsch et al. 2002; Yadav et al. 2019).

PED has some advantages when compared to other electrodeposition techniques, the main ones being the ability to control the amplitude and duration of the applied pulses, as well as the capacity to implement a rest pulse for renewing the concentration of metal ions at the deposition interface, which allows a more homogeneous growth of the nanoarchitectures (Azevedo et al. 2012; Nielsch et al. 2000). However, a drawback of this fabrication method is that the resulting nanostructures have a dendritic structure at one end, which modifies their physical properties and is undesirable for biomedical applications (Sousa et al. 2012a; Furneaux et al. 1989). Other disadvantage of this approach is that a constant current density is applied, which implies that the reaction rate stays constant and the potential (reaction driving force) changes with time, translating into a variation of the NWs composition along their length, when electrodepositing alloys (Llavona et al. 2013; Wang 2003; Yevtushenko 2007). Also, the high potential needed to deposit material, due to the presence of a thin oxide layer at the pore bottom, can lead to a significant hydrogen evolution at the cathode, creating defects along the wire or even inhibiting its growth (Llavona et al. 2013; Wang 2003; Yevtushenko 2007).

The fabrication of FePt nanostructures by other electrodeposition techniques, namely, direct current (DC) or alternating current (AC) electrodeposition, has also been reported. Regarding the first strategy, in some works it was verified that the nanoholes were not filled and a continuous film was formed on top of the template, nevertheless, when material was deposited, the obtained array was considerably heterogeneous (Ilkhchy and Nasirpour 2014; Mori et al. 2009). In order to try to achieve better results, a DC pulsed

electrodeposition technique has been employed, where a negative voltage pulse is applied followed by a pulse of 0 V (Mori et al. 2009). Using this technique, various authors have produced homogeneous arrays of FePt NWs, but an adjustment of the duration of the two pulses was required depending on the diameter of the nanoholes (Mori et al. 2009; Zhang et al. 2013). Arrays of FePt one-dimensional nanostructures with better homogeneity have been produced by AC electrodeposition; however, this technique also led to a variation of the NWs stoichiometry along their length (Ilkhchy and Nasirpour 2014; Fardi-Ilkhchy et al. 2016).

Regarding NWs with a composition gradient along their length, the behaviour of their magnetization can be better understood through micromagnetic simulations. However, a search through the literature reveals that there are still very few works addressing such type of nanostructures. In particular, only two experimental works were found on this specific topic (Aslam et al. 2020; Zeng et al. 2014). Nevertheless, some studies on micromagnetic simulations of NWs with step-like stoichiometry variations along their length were published. For example, Bran et al. 2020 performed micromagnetic simulations to study the magnetic configurations of CoNi/Ni multisegmented cylindrical NWs. In this work, it was noticed that the Ni segments possessed a small magnetization curling at the surface with a chirality that determined the magnetic state of the neighbouring CoNi segments. Particularly, when the CoNi segments were long enough, they possessed a pair of vortices with opposing chirality. On the other hand, when the length of the CoNi segments was reduced, they exhibited a single vortex domain, whose chirality was equal to that of the curling component of magnetization in the neighbouring Ni segments.

A different study by Proenca et al. (2021) analysed the magnetic behaviour of multilayered Au/Ni/Au NW arrays, as well as of individual nanostructures, with different diameters and lengths. Here, it was verified that the magnetostatic interactions together with the shape anisotropy played a key role on the magnetization reversal dynamics in arrays of cylindrical NWs. Particularly, a critical diameter of ≈ 30 nm of Ni determined the type of domain wall generated, while the number of domain walls formed was observed to be dependent on a critical length of about 100 nm. Moreover, the authors verified that the magnetization reversal dynamics were significantly dependent on the NWs' dimensions.

Another work, by Fernandez-Roldan et al. (2020), addressed, through micromagnetic simulations, the domains and domain walls in multisegmented Co/Ni NWs and FeCo NWs with geometrical constrictions along their length. Regarding the later nanostructures, it was verified that the demagnetization occurs through the nucleation of open vortex structures at the constriction, always beginning of the wider segments. On the other hand, when analysing the multisegmented NWs, the authors concluded

that the Co/Ni interface is capable of pinning the domain walls in the course of the magnetization reversal, due to a differential switching of the involved segments.

In this study, we aimed to synthesize FePt NWs through PED into PAA templates and, moreover, analyse the effect of different fabrication parameters on the composition of the resulting nanoarchitectures. Particularly, the influence of the barrier layer thickness and current density on the composition of the produced nanostructures were addressed, having been verified that those parameters allow the control of the Fe:Pt atomic ratio in the obtained nanoarchitectures. Furthermore, magnetic measurements demonstrated that the magnetic hysteresis depended on the composition of the fabricated nanostructures. Moreover, micromagnetic simulations of FePt NW arrays were carried out and compared with the experimental results, in order to gain a better understanding of the magnetization behaviour in these nanostructures.

Experimental procedure

Preparation of nanoporous aluminium oxide templates

Nanoporous alumina templates were prepared through a typical two-step anodization process where, first, an Alfa Aesar high purity aluminium (Al) foil (99.997%) with a thickness of 0.25 mm was cut into squares (1.5×1.5 cm). Subsequently, the Al squares were subjected to a pre-treatment consisting of 3 successive ultrasonic baths of acetone, isopropanol, and ethanol 96%, each with a duration of 3 min. After that process, the Al samples were electropolished at 20 V, during 2 min, in a stirred electrolyte maintained at a temperature of around 10 °C, which was composed of perchloric acid, HClO₄, and ethanol, C₂H₅OH, (volume ratio 1:4). Then, the electropolished Al substrates were anodized in a 0.3 M oxalic acid, (COOH)₂, solution kept at about 2 °C, under a constant potential of 40 V (vs Pt mesh) during 24 h, which was applied using a digital sourcemeter (Keithley 2400) interfacing with LabView software. Subsequently, the Al samples were placed in a mixture of 0.4 M phosphoric acid, H₃PO₄, and 0.2 M chromic acid, H₂CrO₄, at room temperature for 24 h, so as to remove the formed alumina layer. Afterwards, a second anodization was performed on those Al substrates, under the same conditions as the ones considered in the first anodization but considering an anodization time of 8 h. When this process ended, the applied potential was exponentially decreased (non-steady-state anodization) from 40 V down to 8 V or 7 V, in order to reduce the thickness of the alumina barrier layer at the bottom of each nanopore from ≈ 52 nm to ≈ 10.4 nm or ≈ 9.1 nm, according to

$$\delta_b = kV_{ap}, \quad (1)$$

where δ_b is the PAA barrier layer thickness, k (≈ 1.3 nm/V) represents a phenomenological constant, and V_{ap} is the potential applied in the anodization procedure (Sousa et al. 2011).

Electrodeposition of FePt nanowires

FePt NWs were obtained by pulsed electrodeposition into the produced PAA templates (working electrode), using an electrolyte composed of 20 g/L iron (II) sulphate heptahydrate ($\text{FeSO}_4 \cdot 7\text{H}_2\text{O}$), 1 g/L hexachloroplatinic acid hexahydrate ($\text{H}_2\text{PtCl}_6 \cdot 6\text{H}_2\text{O}$), and 30 g/L boric acid (H_3BO_3). This fabrication process was performed at room temperature, using a Keithley 2400 sourcemeter, and it consisted of applying three successive pulses (vs a Pt mesh counter electrode) with different durations (Azevedo et al. 2012, 2014; Sousa et al. 2012a):

- Deposition pulse (8 ms): this pulse has a negative polarization and a constant current density (6–25 mA/cm²), being applied to deposit the material inside the nanopores of the template;
- Discharge pulse (2 ms): this pulse has a positive polarization and is applied to discharge the capacitance associated with the alumina barrier layer, as well as to fix eventual fractures that may appear on the template as a result of the first pulse, enhancing its homogeneity. The potential of this pulse corresponds to the final potential applied during the barrier layer thinning process, i.e. 7 V or 8 V;
- Rest pulse (0.7 s): this pulse has 0 mA and 0 V, being applied to introduce a rest time during which the ion concentration at the deposition interface is replenished and, consequently, to assure a homogeneous concentration of ions along each nanopore prior to the subsequent deposition pulse, thus limiting the hydrogen evolution and enhancing the deposition uniformity.

During the electrodeposition, the deposition voltage and discharge current following each deposition and discharge pulse, respectively, were measured. The deposition times ranged from 5 to 75 min.

Characterization

The morphology and composition of the produced nanostructures were examined through scanning electron microscopy (SEM) and energy dispersive X-ray spectroscopy (EDS), respectively, using a FEI Quanta 400 FEG ESEM/EDAX Genesis X4M instrument. Additionally, the magnetic hysteresis loops ($M(H)$) of the synthesized samples were

obtained at room temperature, considering the external magnetic field (H) applied along the parallel (H_{\parallel}) and perpendicular (H_{\perp}) directions in relation to the NWs' longitudinal axis. These measurements were performed using a vibrating sample magnetometer (VSM), LakeShore Controller Model 7304 (Lake Shore Cryotronics Inc., Westerville, OH, USA), and a Quantum Design/EverCool superconducting quantum interference device (SQUID), MPMS EverCool (Quantum Design Inc., San Diego, CA, USA) magnetometer.

Micromagnetic simulations

Magnetic hysteresis loops of FePt NW arrays were simulated using the Object Oriented Micro-Magnetic Framework (OOMMF) project (Donahue and Porter 1999). Hexagonal arrays of 7 NWs with diameters of 36 nm, centre-to-centre distances of 105 nm, and lengths of 150 nm were studied using a cubic mesh with unit cell size of $3 \times 3 \times 3$ nm³. The saturation magnetization (M_{Sat}) and stiffness constant (A) values were tuned depending on the Fe atomic percentage (at.%) of the FePt NWs studied. Particularly, for NWs with a Fe at.% of 100%, $M_{\text{Sat}} = 1700 \times 10^3$ A/m and $A = 21 \times 10^{-12}$ J/m (according to the bulk values provided by OOMMF). On the other hand, for a Fe at.% of x , $M_{\text{Sat}} = x \times 1700 \times 10^3$ A/m and $A = x \times 21 \times 10^{-12}$ J/m. In all cases, a stopping condition of $|dm/dt| = 1$ deg/ns and a damping factor of 0.015 were considered.

Results and discussion

PAA templates with a thickness of 20 μm , an interpore distance equal to 105 nm, and nanopores with 35 nm in diameter were used to vertically grow FePt NWs through pulsed electrodeposition. The porosity of this type of membranes, which determines the effective electrodeposition area, was studied by Nielsch et al. (2002), who found that the self-ordering in PAA produced through electrochemical anodization requires a porosity of 10% regardless of the considered anodization conditions, which is known as the 10% porosity rule. This porosity value is associated with a volume expansion of aluminium oxide to aluminium equal to ~ 1.2 . However, before the electrodeposition, the thick insulating aluminium oxide layer existing between each nanopore and the Al substrate, which is formed after the second anodization (Fig. 1), has to be thinned, so that electrons can tunnel through it. The thickness of such layer determines the electron flux that occurs during the pulsed electrodeposition process, which allows the metal ions reduction (Sousa et al. 2011). Therefore, it is possible to control the deposition by adjusting such parameter.

In this work, the aluminium oxide barrier layer was thinned by exponentially decreasing the anodization

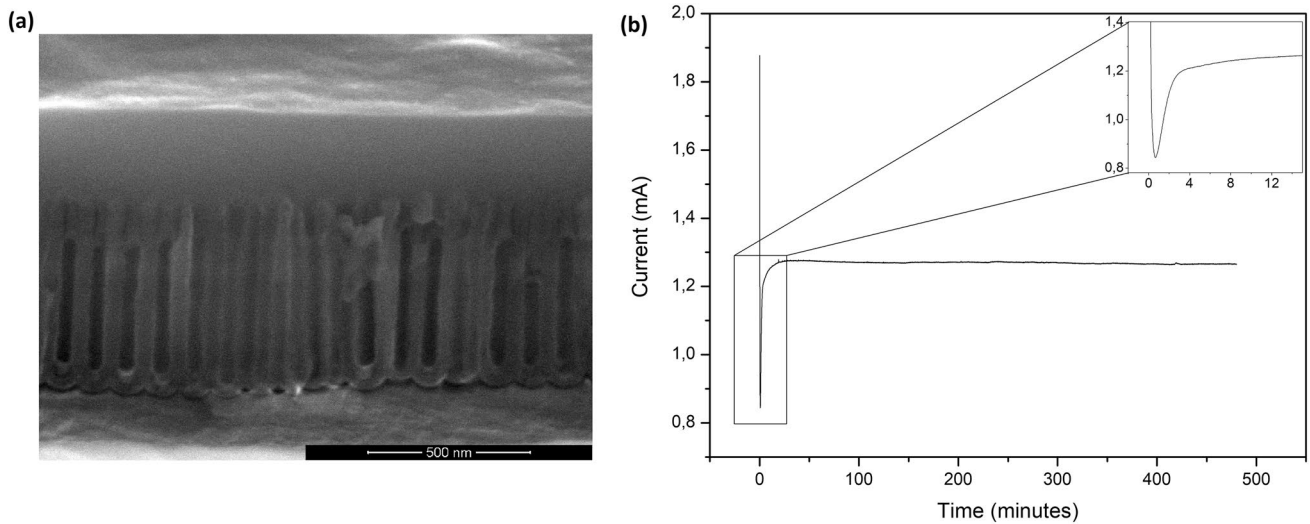


Fig. 1 **a** SEM cross-sectional image of a PAA membrane after the second anodization and **b** corresponding variation of the current with time during its formation. Inset: magnified view of the initial behaviour of the curve. Graphics program used to create the artwork: OriginPro 8.5

potential from 40 V down to 8 V or 7 V, so as to reduce its thickness from ≈ 52 nm to ≈ 10.4 nm or ≈ 9.1 nm (Fig. 2), respectively, and, consequently, analyse the influence of such parameter on the resulting nanostructures. Moreover, this process originated a reproducible tree-like branched structure (also known as dendritic structure) at the bottom of each nanopore. The porosity of the resulting template can be calculated through the following equation (Sousa et al. 2012b):

$$P = \frac{2\pi}{\sqrt{3}} \left[\frac{D_p}{\frac{D_{int}}{2}} \right]^2, \tag{2}$$

where D_p is the pore diameter and D_{int} is the interpore distance.

In the particular case of PAA templates anodized in oxalic acid under 40 V, followed by an anodization potential reduction down to 7 V, their porosity varies from 8 to 10% in the pore region up to 32% in the last generation of dendrites

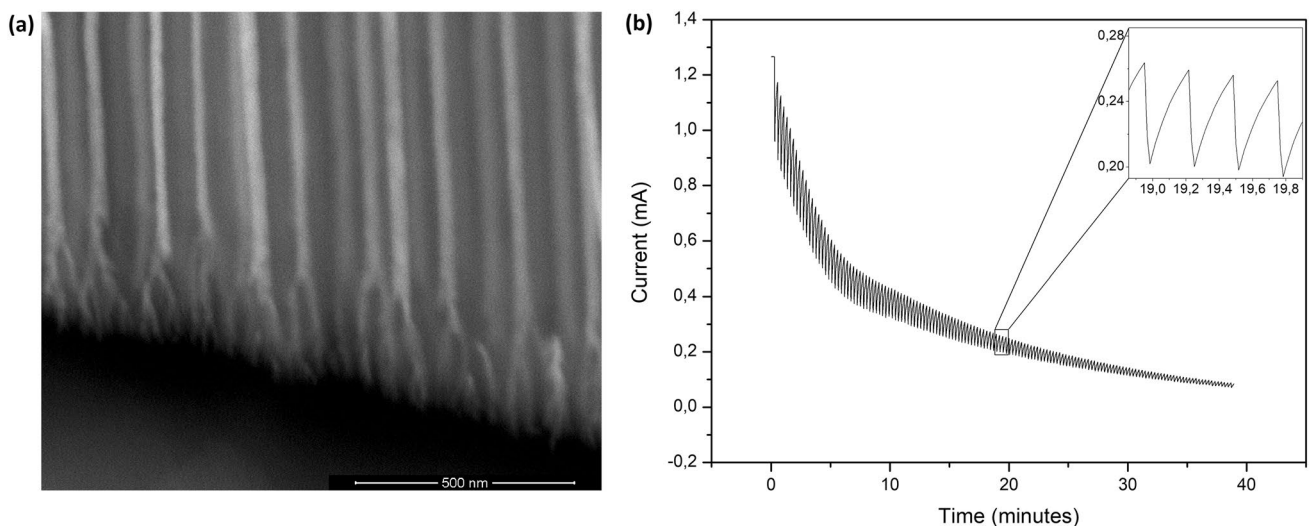


Fig. 2 **a** SEM cross-sectional image of a PAA template filled with electrodeposited FePt NWs evidencing the dendritic structures at the bottom of the nanopores, which resulted from the barrier layer thinning process, and **b** variation of the current with time during the

exponential decrease of the anodization potential (from 40 V down to 7 V). Inset: magnified view of the curve behaviour. Graphics program used to create the artwork: OriginPro 8.5

(Sousa et al. 2012b). This modification in the porosity along the various generations of dendrites directly influences the effective electrodeposition area during the NWs growth. Particularly, as observed in Fig. 3, during the filling of the template section with a constant porosity, which corresponds to the stage IV, the electrodeposition potential (V_{dep}) hardly changes, being rather independent of the deposited nanostructures' length. Nevertheless, in our case, we have a highly diffusion-limited electrodeposition that leads to an increase of the electrodeposition potential and a consequent inhibition of the NW growth, due to the trapping of H_2 bubbles inside the nanopores.

However, during the filling of the dendritic structures at the bottom of the nanopores (Fig. 3; stages I–IV), it is possible to verify that there is an increase of V_{dep} . This occurs due to the change of the effective electrodeposition area associated with the decrease of the local porosity from $\sim 32\%$ to $\sim 10\%$. Moreover, if the deposited nanoarchitectures reach the surface of the template (Fig. 3; stage VII), the deposition area increases rapidly, which translates into a sudden reduction of V_{dep} . Furthermore, if deposition continues, hemispherical caps on top of each NW start to develop, which will ultimately merge, originating a thin film at the surface of the template.

After fabricating the PAA templates, FePt nanostructures were synthesized through pulsed electrodeposition, at a constant current density, into the nanopores of those membranes. In this process, the formation of the desired nanoarchitectures can be divided into four steps (Pauvonic and Schlesinger 2006; Schloerb et al. 2010): (1) Transfer

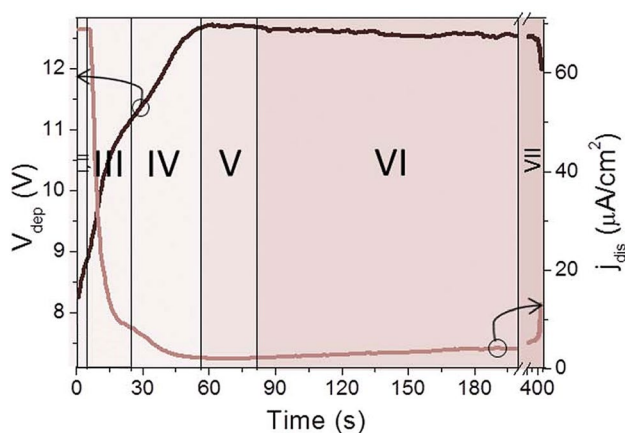


Fig. 3 Behaviour of the electrodeposition potential (V_{dep}) during PED into PAA templates, which possess dendritic structures at the bottom of the nanopores that were generated in a non-steady-state anodization process (j_{dis} represents the current density after each discharge pulse). Adapted from Sousa et al. (2012b). Republished with permission of Royal Society of Chemistry, from Precise control of the filling stages in branched nanopores, Sousa, C. T.; Apolinario, A.; Leitao, D. C.; Pereira, A. M.; Ventura, J.; Araujo, J. P., 22, 2012; permission conveyed through Copyright Clearance Center, Inc

of the metal ions from the bulk electrolyte to the electrode interface; (2) Adsorption of the metal ions on the electrode surface; (3) Charge transfer, originating metal atoms; and (4) Nucleation and growth of the nanostructures.

The nanoporous structure of the template does not influence the last three steps; however, the first one is a mass transport process and, consequently, it is affected by the diameter and length of the nanopores (Mehmood et al. 2017; Schloerb et al. 2010). As a result, the electrodeposition into nanoporous structures is diffusion limited, since the mass transport within the nanopores is limited by the diffusion of metal ions to the electrode surface (Azevedo et al. 2014; Mehmood et al. 2017; Wang 2016). Furthermore, the electrodeposition of less noble metals, such as Fe, is accompanied by hydrogen evolution at the cathode surface, leading to the formation of gaseous H_2 bubbles (Kavner et al. 2008; Zhang et al. 2020). In the case of nanoporous templates, this reaction can inhibit the NW growth, since a bubble can completely fill the pore and, as a result, prevent more metal ions from reaching the electrode surface (Schloerb et al. 2010).

Taking into account these effects, different current densities were considered in order to analyse the effect of such parameter on the resulting nanoarchitectures. The obtained samples were analysed through SEM in order to evaluate the NWs length and homogeneity. As observed in Fig. 2, despite the dendrites at the bottom of the template being homogeneously filled, the electrodeposited nanostructures presented varying lengths. This result was more evident for the cases where current densities lower than 40 mA/cm^2 were considered (Fig. 4a). On the other hand, for higher current densities, the template filling was considerably more homogeneous (Fig. 4b).

Then, the fabricated samples were analysed by EDS, so as to determine the composition of the electrodeposited nanoarchitectures. As a result, when considering a barrier layer thickness of $\approx 10.4 \text{ nm}$, it was verified that only Pt was present in the resulting nanoarchitectures, regardless of the applied current density ($12\text{--}70 \text{ mA/cm}^2$). On the other hand, when thinning the barrier layer down to $\approx 9.1 \text{ nm}$, the EDS analysis (Fig. 5) revealed that at low current densities only Pt was electrodeposited, but as the current density increased, the percentage of that element in the fabricated samples decreased and the Fe percentage increased until only Fe was electrodeposited at the higher current densities.

From Fig. 5, we can verify that for current densities lower than 7 mA/cm^2 only Pt is deposited, at very low deposition rates (15 min to grow 227 nm). The percentage of Fe in the NWs increases *quasi* linearly with this parameter up to $\text{Fe}_{80}\text{Pt}_{20}$; however, for current densities higher than 40 mA/cm^2 only Fe is deposited. These compositional results, as well as those regarding the AAO templates filling, are in accordance with the ones reported in the literature (Fardi-Ilkhchy et al. 2016).

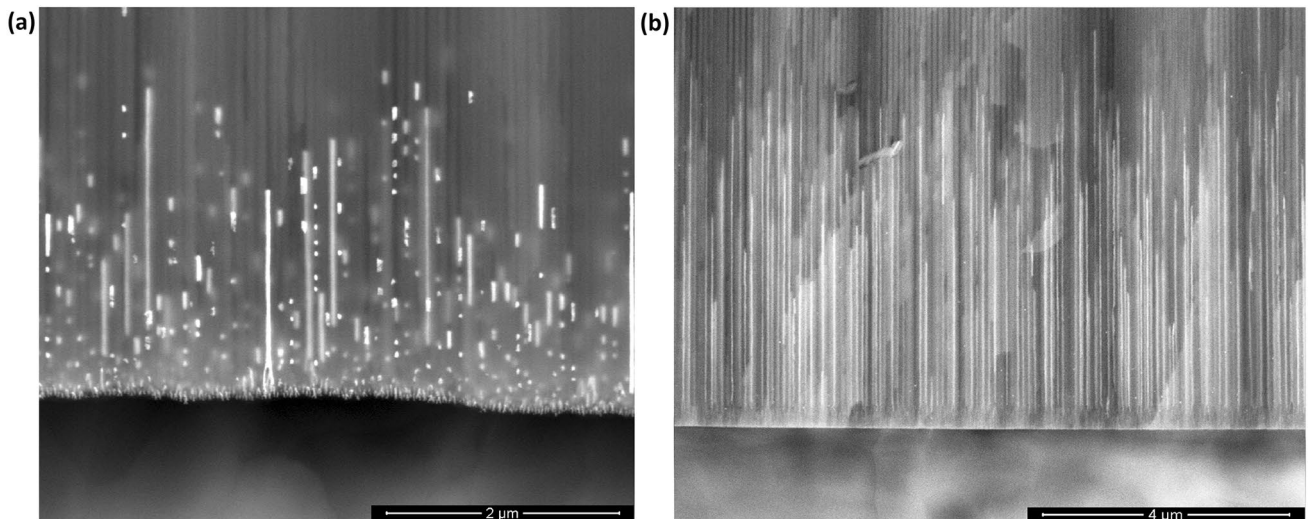


Fig. 4 SEM images of the samples electrodeposited at **a** 6 mA/cm² and **b** 40 mA/cm², considering a barrier layer thickness of ≈ 9.1 nm

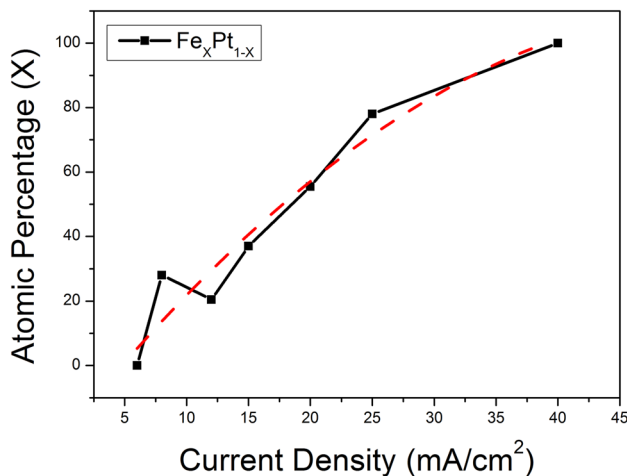


Fig. 5 Atomic percentage of Fe and Pt as a function of the electrodeposition current density, when considering a barrier layer thickness of ≈ 9.1 nm. The dashed red line is a polynomial trend line fitted to the acquired data and a guide to the eye. Graphics program used to create the artwork: OriginPro 8.5

Therefore, it is possible to conclude that both the barrier layer thickness and the current density applied during the electrodeposition process influence the composition of the resulting FePt nanostructures, allowing a control over the atomic percentage of the two elements involved.

Afterwards, the parallel and perpendicular hysteresis loops of the synthesized NW arrays were measured at room temperature using a VSM, as well as a SQUID (Fig. 6). In that figure, the anisotropy field distribution (AFD) curves are also represented. These were determined, for each sample, by performing a cubic b-spline interpolation of the descendant branch of the hard axis

hysteresis loop (perpendicular orientation) from the positive saturation down to the remanence value, then calculating the second derivative of the resulting data, and finally performing the following operation for each point (H_A) (Vega et al. 2012a, b; Fernández 2014):

$$\sigma(H_A) = -H \frac{d^2}{dH^2} \langle M(H) \rangle \Big|_{H=H_A}, \tag{3}$$

where $\sigma(H_A)$ is the AFD value at point H_A , H is the external magnetic field, and $M(H)$ is the magnetization of the sample when the magnetic field is H .

Based on the acquired data, it is possible to conclude that the nanostructures' easy magnetization axis is parallel to their longitudinal axis. Additionally, it is observed a significant increase of the magnetic hysteresis as the current density applied during the fabrication process gets higher. Furthermore, we can also verify that the increase of such electrodeposition parameter originates samples with a larger remanent magnetization in both orientations, being, such dependence, more significant in the parallel orientation. Another relevant property of these materials is their coercivity, or coercive field, H_c . From Fig. 6, it is noticeable that the coercivity of the samples synthesized under higher current densities is larger in the two considered orientations, when compared to those produced by applying a lower current density. Additionally, and in similar fashion to the remanent magnetization, the variation of the coercivity is more pronounced for the parallel orientation.

These results, regarding the magnetic hysteresis, remanent magnetization, and coercivity of the fabricated nanoarchitectures, can be attributed to the fact that the Fe at.%

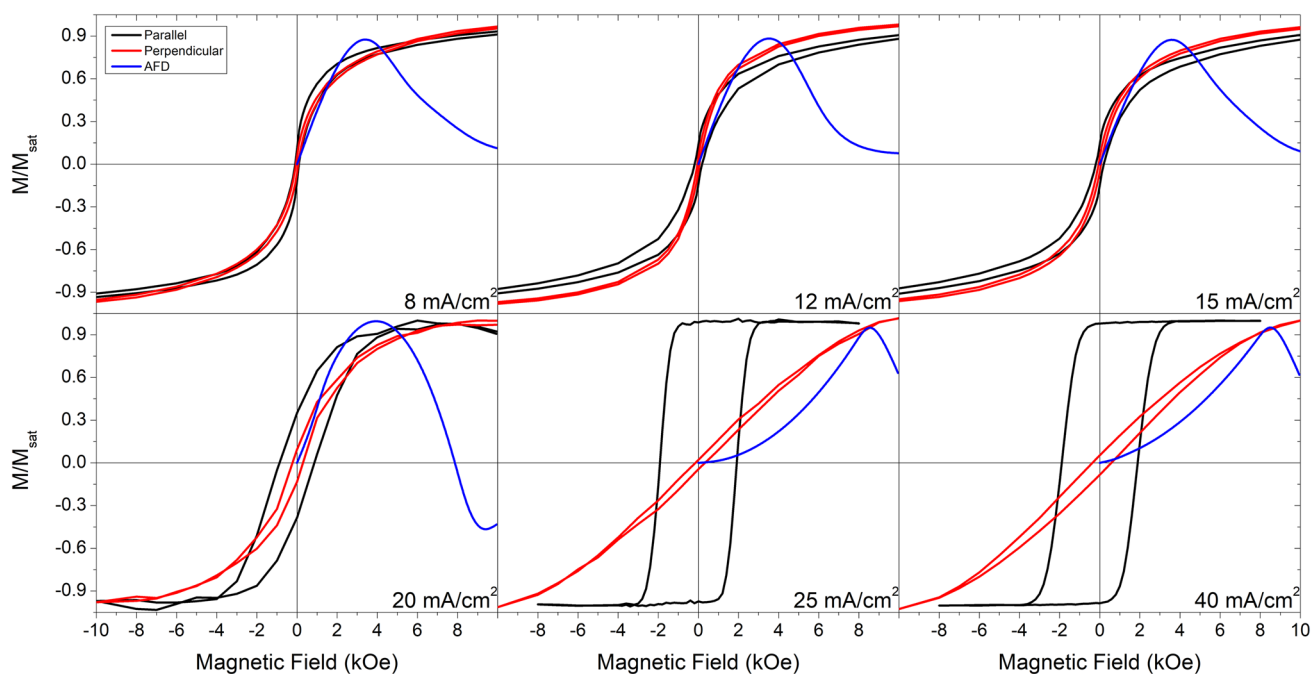


Fig. 6 Parallel and perpendicular hysteresis loops and AFD curves of the samples electrodeposited at 8, 12, 15, 20, 25, and 40 mA/cm². Graphics program used to create the artwork: OriginPro 8.5

in the nanostructures is larger when higher current densities are applied, as observed in the EDS analysis.

Another important parameter of the fabricated samples is the mean anisotropy field ($\langle H_A \rangle$), or perpendicular saturation field (H_{Sat}^\perp), which is the minimum magnetic field required to saturate the magnetization of a material along its hard axis direction (Mukhtar et al. 2019; Tameerug 2000; Shepley 2015; Nowick 1973). Such field can be determined from the calculated AFD curves, since it corresponds to the magnetic field at which that curve reaches its maximum (Fernández 2014; Méndez et al. 2017). The H_{Sat}^\perp values obtained through this method are illustrated in Fig. 8a, where it is possible to verify that such field increases as the Fe at.% in the fabricated nanostructures gets higher.

The magnetic hysteresis loops of an array of 7 NWs with different Fe_xPt_{1-x} stoichiometries were also simulated by applying the magnetic field parallel and perpendicular to the NWs' long axis. The Fe at.% values simulated were 30%, 55%, and 100%, always considering a uniform distribution of Fe along the NWs' length.

As a result, it was verified that the hysteresis loops simulated for the 100% Fe NWs arrays illustrated a similar behaviour when compared to the ones experimentally measured (Fig. 7a). Furthermore, as the Fe at.% got lower, it was observed a reduction of the perpendicular saturation field values in both the simulated and experimentally measured hysteresis loops (refer to Fig. 8a). However, when analysing the simulated parallel hysteresis loops for Fe at.% of 55%

and 30% and comparing them to the experimental ones, the differences were noticeable. Specifically, much higher coercivity values were obtained in the calculated loops (refer to Fig. 8b). This might be ascribed to the inhomogeneous length distribution of the NWs array deposited at smaller current densities, as observed in the SEM images (Fig. 4). In addition, slight differences in the FePt stoichiometry along the NWs' length were also found by EDS, as usually occurs when using PED techniques inside long and narrow nanoporous templates. In particular, the dendrites present at the bottom of the wires appeared to have less Fe at.% than the rest of the nanostructure.

To better understand the effect of a possible change in stoichiometry along the samples, a NW array with a change in stoichiometry along the wires' length was also simulated. In this case, the NWs length was divided into 5 equal parts (each with 30 nm in thickness) and the Fe at.% was set to 10%, 20%, 30%, 40%, and 50% at each consecutive segment. As a result, the simulated parallel hysteresis loop evidenced a decrease in coercivity when compared to the ones simulated for Fe at.% of 30% and 55% (Fig. 8b). This result confirms the important effect that stoichiometry has in the magnetization reversal process of FePt NWs. Further analysis of their magnetic configuration using OOMMF revealed that the reversal of the magnetization in FePt NW arrays with a gradient stoichiometry occurred by the nucleation of a transverse domain wall at the segment with the lowest Fe at.%, which then propagated along the neighbouring

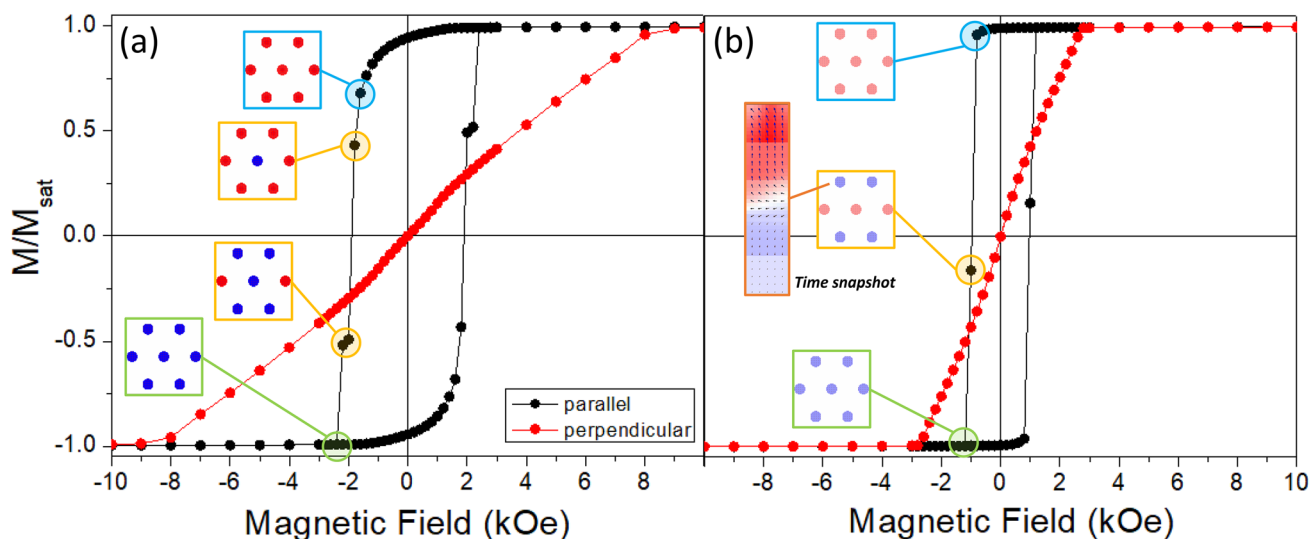


Fig. 7 Simulated magnetic hysteresis loops of an array of 7 FePt NWs with an Fe at.% of **a** 100% and **b** 10–20–30–40–50% (gradient), obtained by applying the magnetic field parallel and perpendicular to the NWs’ long axis. Insets show cross-sectional views of the

magnetic configurations at specific applied fields, with a colour scale of red ($M^{\parallel}/M_{\text{Sat}} = 1$), white ($M^{\parallel}/M_{\text{Sat}} = 0$), and blue ($M^{\parallel}/M_{\text{Sat}} = -1$), where M^{\parallel} is the magnetization along the NWs’ long axis. Graphics program used to create the artwork: OriginPro 8.5

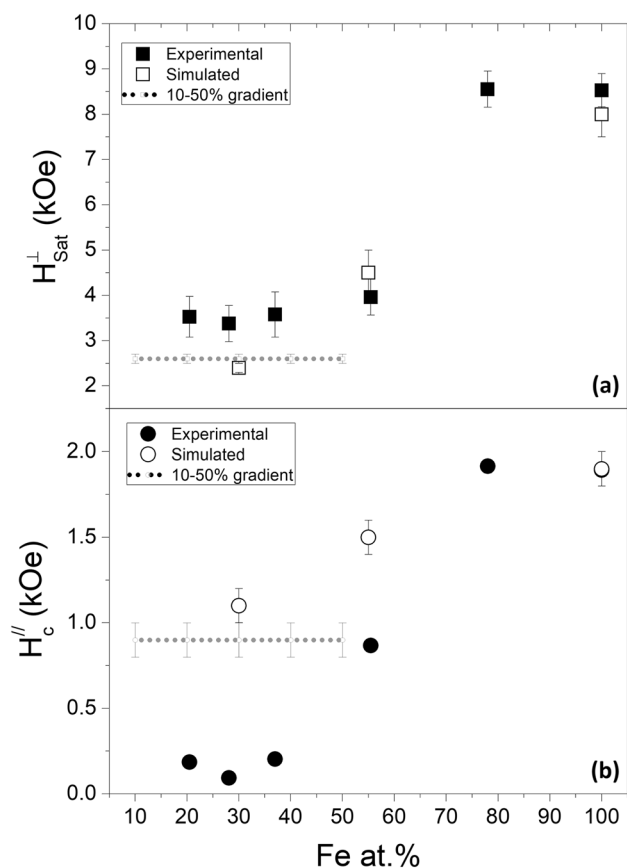


Fig. 8 Experimental and simulated **a** H_{Sat}^{\perp} , and **b** parallel coercive field, H_c^{\parallel} . Graphics program used to create the artwork: OriginPro 8.5

segments (refer to time snapshot in Fig. 7b). This led to a reduction of the parallel coercivity, as observed in the simulated parallel hysteresis loops (Fig. 7b).

In summary, the micromagnetic simulation results suggest that FePt NWs deposited at lower current densities might have regions with lower Fe at.%, which induce the reversal of the NWs magnetization at smaller magnetic field values. Therefore, the much lower parallel coercivities experimentally measured might be ascribed to existence of nucleation sites along the NWs’ length with a lower Fe at.%.

By comparing these results with those from a study where micromagnetic simulations of NWs composed of two different Fe alloys were performed, it is possible to verify the existence of some similarities. Particularly, Aravindh et al. (2012) verified that the magnetic moment and coercive field of $\text{Fe}_{(1-x)}\text{M}_x$ ($\text{M} = \text{Co/Ni}$) NWs monotonically decreased with the content of Co or Ni. A similar effect was observed in our work, where the lowering of the Fe at.% in the FePt nanostructures reduced those two properties of the NWs. The authors of such paper also verified that the Co, or Ni, content influenced the orientation of the easy axis of magnetization of the analysed nanoarchitectures, however, in this work, Pt did not seem have such effect.

Conclusions and future work

In summary, we demonstrated a method for fabricating FePt nanostructures involving pulsed electrodeposition into nanoporous alumina templates. With this technique, it is possible to control the composition of the

nanoarchitectures by adjusting the thickness of the barrier layer at the bottom of the template and the current density applied during the electroplating process. Nevertheless, the length of the NWs grown at lower current densities is not homogeneous. Furthermore, the magnetic characterization of the obtained samples revealed that there is a considerable increase of the magnetic hysteresis with the increase of the current density applied during the electro-deposition procedure. Additionally, micromagnetic simulations of FePt NW arrays with various stoichiometries indicated that the nanostructures produced at lower current densities may possess a varying stoichiometry along their length.

Therefore, regarding future work, we pretend to fabricate FePt NWs with more uniform length and possessing a homogeneous composition along their length. For such purpose, we are currently trying to synthesize this type of nanostructures using the same kind of template, but considering a different electrodeposition technique where a constant potential is applied, i.e. potentiostatic DC electrodeposition.

Authors contributions All the authors contributed to the study conception and design. RM and CTS contributed to conceptualization and formal analysis; RM and MPP were involved in methodology; MPP performed magnetic simulations; CN and JPA did validation; JPA, MPP, and C.T.S. contributed to resources; RM was involved in writing original draft preparation; CS and MPP were involved in writing—review and editing; CTS and CN performed supervision; CTS contributed to project administration; JPA and CTS were involved in funding acquisition. All the authors have read and agreed to the published version of the manuscript.

Funding This work was supported by Portuguese *Fundação para a Ciência e Tecnologia* (FCT) and *Programa Operacional Regional Norte (Fundo Social Europeu)* under the project SFRH/BD/148563/2019 and IF/01159/2015. This work was also financially supported by the FCT and Programa Operacional Competitividade e Internacionalização 2020 (Fundo Europeu de Desenvolvimento Regional) under the projects POCI-01-0141-FEDER-032527, PTDC/FIS-MAC/31302/2017, PTDC/CTM-CTM/28676/2017, PTDC/FIS-OTI/32257/2017, and Strategic Funding contract UIDB/04968/2020, from the Spanish *Ministerio de Ciencia e Innovación* under the project PID2020-117024GB-C42, and from European Union's Horizon 2020 research and innovation programme under the Marie Skłodowska-Curie Grant Agreement No. 734801. This work has also made use of the Spanish ICTS Network MICRONANOFABS.

Availability of data and material Not applicable: data sharing not applicable to this article as no datasets were generated or analysed during the current study.

Code availability Not applicable.

Declarations

Conflict of interest On behalf of all authors, the corresponding author states that there is no conflict of interest.

References

- Aravindh SA, Jaya SM, Valsakumar MC, Sundar CS (2012) Compositional variation of magnetic moment, magnetic anisotropy energy and coercivity in Fe(1-x) Mx (M= Co/Ni) nanowires: an ab initio study. *Appl Nanosci* 2:409–415. <https://doi.org/10.1007/s13204-011-0053-9>
- Aslam S, Das A, Khanna M, Kuanr BK (2020) Concentration gradient Co-Fe nanowire arrays: microstructure to magnetic characterizations. *J Alloy Compd* 838:155566. <https://doi.org/10.1016/j.jallcom.2020.155566>
- Azevedo J, Sousa CT, Mendes A, Araújo J (2012) Influence of the rest pulse duration in pulsed electrodeposition of Fe nanowires. *J Nanosci Nanotechnol* 12:9112–9117. <https://doi.org/10.1166/jnn.2012.6769>
- Azevedo J, Sousa CT, Ventura J, Apolinario A, Mendes A, Araújo J (2014) Ultra-long Fe nanowires by pulsed electrodeposition with full filling of alumina templates. *Mater Res Express* 1:015028. <https://doi.org/10.1088/2053-1591/1/1/015028>
- Bran C, Fernandez-Roldan JA, Del Real RP, Asenjo A, Chen YS, Zhang J, Zhang X, Rodríguez AF, Foerster M, Aballe L, Chubykalo-Fesenko O, Vazquez M (2020) Unveiling the origin of multidomain structures in compositionally modulated cylindrical magnetic nanowires. *ACS Nano* 14:12819–12827. <https://doi.org/10.1021/acsnano.0c03579>
- Casillas PEG, Olivas-Armendariz I, Gonzalez C, Castrejón-Parga K, Pérez CM (2015) Magnetic nanostructures for biomedical applications. In: Fraceto LF, de Araújo DR (eds) *Microspheres*. Nova Science Publishers, New York, pp 137–160
- Chiriac H, Radu E, Țibu M, Stoian G, Ababei G, Lăbușcă L, Herea D-D, Lupu N (2018) Fe-Cr-Nb-B ferromagnetic particles with shape anisotropy for cancer cell destruction by magnetomechanical actuation. *Sci Rep* 8:1–9. <https://doi.org/10.1038/s41598-018-30034-3>
- Crisan O, Dan I, Palade P, Crisan A, Leca A, Pantelica A (2020) Magnetic phase coexistence and hard-soft exchange coupling in FePt nanocomposite magnets. *Nanomaterials* 10:1618. <https://doi.org/10.3390/nano10081618>
- Domracheva N, Caporali M, Rentschler E (2018) *Novel Magnetic nanostructures: unique properties and applications*. Elsevier, Amsterdam
- Donahue MJ, Porter D (1999) *OOMMF user's guide, version 1.0*. US Department of Commerce, National Institute of Standards and Technology
- Elkins K, Li D, Poudyal N, Nandwana V, Jin Z, Chen K, Liu JP (2005) Monodisperse face-centred tetragonal FePt nanoparticles with giant coercivity. *J Phys D Appl Phys* 38:2306. <https://doi.org/10.1088/0022-3727/38/14/003>
- Elmiladi NM (2010) Proton spin-lattice relaxation in colloidal aqueous solutions with resonant ultrasound. Dissertation, Rheinische Friedrich-Wilhelms-Universität Bonn
- Ertan A, Tewari SN, Talu O (2008) Electrodeposition of nickel nanowires and nanotubes using various templates. *J Exp Nanosci* 3:287–295. <https://doi.org/10.1080/17458080802570617>
- Faivre D (2016) *Iron oxides: from nature to applications*. Wiley-VCH, Weinheim
- Fardi-Ilkhchy A, Nasirpouri F, Bran C, Vázquez M (2016) Compositionally graded Fe(1-x)-Pt(x) nanowires produced by alternating current electrodeposition into alumina templates. *J Solid State Chem* 244:35–44. <https://doi.org/10.1016/j.jssc.2016.08.016>
- Fernández JG (2014) Magnetization processes in transition metal based nanowire arrays. Dissertation, Universidad de Oviedo
- Fernandez-Roldan JA, Ivanov YP, Chubykalo-Fesenko O (2020) Micromagnetic modeling of magnetic domain walls and

- domains in cylindrical nanowires. In: Vázquez M (ed) Magnetic nano- and microwires. Woodhead Publishing, Cambridge, pp 403–426
- Furneaux R, Rigby W, Davidson A (1989) The formation of controlled-porosity membranes from anodically oxidized aluminium. *Nature* 337:147–149. <https://doi.org/10.1038/337147a0>
- Gao Y, Liu Y, Xu C (2014) Magnetic nanoparticles for biomedical applications: from diagnosis to treatment to regeneration. In: Cai W (ed) Engineering in translational medicine. Springer-Verlag, London, pp 567–583
- Ha Y, Ko S, Kim I, Huang Y, Mohanty K, Huh C, Maynard JA (2018) Recent advances incorporating superparamagnetic nanoparticles into immunoassays. *ACS Appl Nano Mater* 1:512–521. <https://doi.org/10.1021/acsnm.7b00025>
- Hanson M, Kazakova O, Blomqvist P, Wäppling R (2002) Submicron particles of Fe/Co multilayers: influence of interactions. *J Appl Phys* 91:7044–7046. <https://doi.org/10.1063/1.1447491>
- Hanusa TP (2015) The lightest metals: science and technology from lithium to calcium. John Wiley & Sons, West Sussex
- Hu F, Joshi HM, Dravid VP, Meade TJ (2010) High-performance nanostructured MR contrast probes. *Nanoscale* 2:1884–1891. <https://doi.org/10.1039/c0nr00173b>
- Ilkhchy AF, Nasirpour F (2014) Effect of barrier layer on fabrication of FePt nanowires by electrodeposition into nanoporous alumina templates. In: Parsa MH (ed) Ultrafine grained and nano-structured materials IV. Trans Tech Publications Ltd, Switzerland, pp 707–711
- Janocha H (2007) Adaptronics and smart structures: basics, materials, design, and applications. Springer, Berlin/Heidelberg
- Jokar A, Ramazani A, Almasi-Kashi M, Montazer A (2016) The roles of temperature and thickness of barrier layer in the electrodeposition efficiency of nickel inside anodic alumina templates. *J Mater Sci: Mater Electron* 27:3995–4002. <https://doi.org/10.1007/s10854-015-4253-z>
- Kadiri VM, Bussi C, Holle AW, Son K, Kwon H, Schütz G, Gutierrez MG, Fischer P (2020) Biocompatible magnetic micro- and nanodevices: fabrication of FePt nanopropellers and cell transfection. *Adv Mater* 32:2001114. <https://doi.org/10.1002/adma.202001114>
- Kanaan DB (2011) Naked singularity: the heart-science of infinite consciousness. Universe, Indiana
- Kavner A, John S, Sass S, Boyle E (2008) Redox-driven stable isotope fractionation in transition metals: application to Zn electroplating. *Geochim Cosmochim Acta* 72:1731–1741. <https://doi.org/10.1016/j.gca.2008.01.023>
- Kesari K (2019) Networking of mutagens in environmental toxicology. Springer Nature Switzerland AG, Gewerbestrasse
- Li Q (2015) In vitro, non-invasive imaging and detection of single living mammalian cells interacting with bio-nano-interfaces. Dissertation, Utah State University
- Llavona A, Pérez L, Sánchez MC, de Manuel V (2013) Enhancement of anomalous codeposition in the synthesis of Fe–Ni alloys in nanopores. *Electrochim Acta* 106:392–397. <https://doi.org/10.1016/j.electacta.2013.05.116>
- Mansor AF, Azmi AI, Zain MZM, Jamaluddin R (2020) Parametric evaluation of electrical discharge coatings on nickel-titanium shape memory alloy in deionized water. *Heliyon* 6:e04812. <https://doi.org/10.1016/j.heliyon.2020.e04812>
- Mehmood T, Mukhtar A, Khan BS, Saeed A, Ahmad W, Kaiming W (2017) Electrochemical process and phase formation of Fe-based alloy nanowires into anodic alumina oxide. *Int J Electrochemical Sci* 12:1203–1215. <https://doi.org/10.20964/2017.02.45>
- Meier LA, Alvarez AE, Garcia S, del Barrio MC (2015) Formation of Cu and Ni nanowires by electrodeposition. *Procedia Mater Sci* 8:617–622. <https://doi.org/10.1016/j.mspro.2015.04.116>
- Méndez M, González S, Vega V, Teixeira JM, Hernando B, Luna C, Prida VM (2017) Ni-Co alloy and multisegmented Ni/Co nanowire arrays modulated in composition: structural characterizations and magnetic properties. *Curr Comput-Aided Drug Des* 7:66. <https://doi.org/10.3390/cryst7030066>
- Mora B, Perez-Valle A, Redondo C, Boyano MD, Morales R (2018) Cost-effective design of high-magnetic moment nanostructures for biotechnological applications. *ACS Appl Mater Interfaces*. <https://doi.org/10.1021/acsnami.7b16779>
- Mori H, Korenaga T, Hosomi N, Terui T, Shingubara S (2009) Filling of FePt in AAO nanohole array by DC pulsed electrodeposition. *ECS Trans* 16:65–71. <https://doi.org/10.1149/1.3140011>
- Mota LM, Nicomedes DNN, Barboza APM, de Moraes Ramos SLL, Vasconcellos R, Medrado NV, de Alvarenga EC, Machado G, Juste KRC, de Vasconcelos CK, Righi A, Manhobosco SM, Resende RR, Batista RJ, Soares JS, Manhobosco TM (2020) Soapstone reinforced hydroxyapatite coatings for biomedical applications. *Surf Coat Technol* 397:126005. <https://doi.org/10.1016/j.surfcoat.2020.126005>
- Mukhtar F, Riaz S, Awan A, Rubab F, Kayani ZN, Naseem S (2019) Structural and magnetization crossover in electrodeposited FeAl₂O₄—effect of *in situ* oxidation. *RSC Adv* 9:38183–38194. <https://doi.org/10.1039/C9RA04455H>
- Niensch K, Müller F, Li A-P, Gösele U (2000) Uniform nickel deposition into ordered alumina pores by pulsed electrodeposition. *Adv Mater* 12:582–586. [https://doi.org/10.1002/\(SICI\)1521-4095\(200004\)12:8%3c582::AID-ADMA582%3e3.0.CO;2-3](https://doi.org/10.1002/(SICI)1521-4095(200004)12:8%3c582::AID-ADMA582%3e3.0.CO;2-3)
- Niensch K, Choi J, Schwirn K, Wehrspohn RB, Gösele U (2002) Self-ordering regimes of porous alumina: the 10% porosity rule. *Nano Lett* 2:677–680. <https://doi.org/10.1021/nl025537k>
- Nowick A (1973) Rare earth permanent magnets. Academic Press, New York
- Peixoto LT (2018) Magnetic nanostructures for biotechnological applications. Dissertation, Faculdade de Ciências da Universidade do Porto
- Proença MP, Rial J, Araujo JP, Sousa CT (2021) Magnetic reversal modes in cylindrical nanostructures: from disks to wires. *Sci Rep* 11:10100. <https://doi.org/10.1038/s41598-021-89474-z>
- Pucci C, Martinelli C, Ciofani G (2019) Innovative approaches for cancer treatment: current perspectives and new challenges. *Ecancermedicalscience* 13:961. <https://doi.org/10.3332/ecancer.2019.961>
- Sandaker B, Eggen A, Cruvellier M (2019) The structural basis of architecture. Taylor & Francis, Oxfordshire
- Schloerb H, Haehnel V, Khatri MS, Srivastava A, Kumar A, Schultz L, Faehler S (2010) Magnetic nanowires by electrodeposition within templates. *Phys Status Solidi B* 247:2364–2379. <https://doi.org/10.1002/pssb.201046189>
- Schwerdt JI, Goya GF, Calatayud MP, Hereñú CB, Reggiani PC, Goya RG (2012) Magnetic field-assisted gene delivery: achievements and therapeutic potential. *Curr Gene Ther* 12:116–126. <https://doi.org/10.2174/156652312800099616>
- Shepley PM (2015) Effect of piezoelectric strain on the magnetic properties of Pt/Co thin films. Dissertation, University of Leeds
- Sousa CT, Leitao DC, Proença MP, Apolinário A, Correia JG, Ventura J, Araújo J (2011) Tuning pore filling of anodic alumina templates by accurate control of the bottom barrier layer thickness. *Nanotechnology* 22:315602. <https://doi.org/10.1088/0957-4484/22/31/315602>
- Sousa CT, Leitao DC, Ventura J, Tavares PB, Araújo JP (2012a) A versatile synthesis method of dendrites-free segmented nanowires with a precise size control. *Nanoscale Res Lett*. <https://doi.org/10.1186/1556-276X-7-168>
- Sousa CT, Apolinario A, Leitao DC, Pereira AM, Ventura J, Araujo JP (2012b) Precise control of the filling stages in branched nanopores. *J Mater Chem* 22:3110–3116. <https://doi.org/10.1039/C2JM14828E>
- Spagnuolo PA (2020) Nutraceuticals and human health: the food-to-supplement paradigm. Royal Society of Chemistry, London

- Stepniowski WJ, Salerno M (2014) Fabrication of nanowires and nanotubes by anodic alumina template-assisted electrodeposition. In: Ahmed W, Ali N (eds) Manufacturing nanostructures. One Central Press, Manchester, pp 321–357
- Sun L, Hao Y, Chien C-L, Searson PC (2005) Tuning the properties of magnetic nanowires. *IBM J Res Dev* 49:79–102. <https://doi.org/10.1147/rd.491.0079>
- Tameerug P (2000) Enhanced AMR in thin Ni₈₀Fe₂₀ film using (Ni₈₀Fe₂₀)₅₆Cr₄₄ or Ni₅₈Cr₄₂ underlayer. Dissertation, San Jose State University
- Thanou M (2018) Theranostics and image guided drug delivery. Royal Society of Chemistry, London
- Thorat N, Bauer J (2020) Nanomedicines for breast cancer theranostics. Elsevier Science, Amsterdam
- Tran N, Webster TJ (2010) Magnetic nanoparticles: biomedical applications and challenges. *J Mater Chem* 20:8760–8767. <https://doi.org/10.1039/C0JM00994F>
- Vashist A, Kaushik AK, Ahmad S, Nair M (2018) Nanogels for biomedical applications. Royal Society of Chemistry, London
- Vega V, Böhnert T, Martens S, Waleczek M, Montero-Moreno JM, Görlitz D, Prida V, Nielsch K (2012a) Tuning the magnetic anisotropy of Co–Ni nanowires: comparison between single nanowires and nanowire arrays in hard-anodic aluminum oxide membranes. *Nanotechnology* 23:465709. <https://doi.org/10.1088/0957-4484/23/46/465709>
- Vega V, Rosa W, García J, Sanchez T, Santos J, Béron F, Pirota K, Prida V, Hernando B (2012b) Template-assisted CoPd nanowire arrays: magnetic properties and FORC analysis. *J Nanosci Nanotechnol* 12:4736–4743. <https://doi.org/10.1166/jnn.2012.4908>
- Wang Q (2003) Anodic electrochemical synthesis and characterizations of nanocrystalline cerium oxide and cerium oxide/montmorillonite nanocomposites. Dissertation, University of North Texas
- Wang C-C (2016) Verification of electrodeposition patterns caused by interfacial instability. Dissertation, University of Florida
- Wang C, Hou Y, Kim J, Sun S (2007) A general strategy for synthesizing FePt nanowires and nanorods. *Angew Chem Int Ed* 46:6449–6451. <https://doi.org/10.1002/anie.200702001>
- Whitehead N (2020) Making the Grade: Generating & Controlling Spin Waves with a Graded Refractive Index. Dissertation, University of Exeter
- Wu K, Su D, Liu J, Wang J-P (2019) Estimating saturation magnetization of superparamagnetic nanoparticles in liquid phase. *J Magn Magn Mater* 471:394–399. <https://doi.org/10.1016/j.jmmm.2018.10.008>
- Xiao Y, Du J (2020) Superparamagnetic nanoparticles for biomedical applications. *J Mater Chem B* 8:354–367. <https://doi.org/10.1039/C9TB01955C>
- Yadav A, Bobji M, Bull SJ (2019) Controlled growth of highly aligned Cu nanowires by pulse electrodeposition in nanoporous alumina. *J Nanosci Nanotechnol* 19:4254–4259. <https://doi.org/10.1166/jnn.2019.16868>
- Yevtushenko O (2007) Electrocrystallization and characterizations of nanostructured gold and gold alloys. Dissertation, Universität des Saarlandes
- Zeng M, Yang H, Liu J, Yu R (2014) Gradient magnetic binary alloy nanowire. *J Appl Phys* 115:17B514. <https://doi.org/10.1016/j.jallcom.2020.155566>
- Zhang S, Zhao D (2017) Advances in magnetic materials: processing, properties, and performance. CRC Press, Florida
- Zhang J, Tong WM, Ding H, Wang HB, Wang H (2013) Fe-Pt alloy nanowire arrays prepared by Pulse DC electrodeposition. *Integr Ferroelectr* 141:24–31. <https://doi.org/10.1080/10584587.2013.778721>
- Zhang Z, Kitada A, Fukami K, Yao Z, Murase K (2020) Electrodeposition of an iron thin film with compact and smooth morphology using an ethereal electrolyte. *Electrochim Acta* 348:136289. <https://doi.org/10.1016/j.electacta.2020.136289>

Publisher's Note Springer Nature remains neutral with regard to jurisdictional claims in published maps and institutional affiliations.